POLITECNICO DI MILANO
Corso di Laurea Magistrale in Ingegneria Biomedica
Dipartimento di Elettronica, Informazione e Bioingegneria

Automatic quantitative susceptibility mapping for iron accumulation assessment in motor neuron disease

Relatore: Prof. Anna Maria Bianchi
Correlatore: Ing. Valeria Elisa Contarino

Tesi di Laurea di:
Luis Carlos Sanmiguel Serpa 876882

Anno Accademico 2017-2018

To all my family and friends for their support in all these years of studies

Summary

Motor Neuron Disease (MND) is a rapidly progressive neurodegenerative disorder characterized by degeneration of upper and/or lower motor neurons associated to iron overload in the brain. This fatal pathology is evenly distributed over the world with high mortality rates.
We implemented a fully automatic pipeline able to analyze Magnetic Resonance images to quantify susceptibility in the motor cortex. Processing included FreeSurfer automatic segmentation of the brain and quantitative susceptibility mapping with Streaking artifact reduction algorithm. Both susceptibility skewness in gray matter and mean susceptibility measurements in adjacent white matter showed sensibility to anomalies in MND. Furthermore, mean susceptibility in subcortical white matter correlated with disease duration and clinical functional score.
The here presented pipeline might be easily adapted to automatically quantify susceptibility in several brain regions, in MND or any other neurodegenerative disease.

Acknowledgements

Firstly I would like to thank to my supervisors Ing. Valeria Contarino and Prof. Anna Maria Bianchi for giving me the opportunity to participate in this project. Their support was fundamental to develop this work. Thus, I want to thank to both institutions *Politecnico di Milano* and *Policlinico di Milano* which are institutions where I as an electronic engineer, have learned a huge set of knowledge in Biomedical engineering, signal processing and medical imaging. Moreover in these institutions I found all the material and support to develop this project.

I would like to thank my friends here in Milan, who became a family for me, for their support in these two years. Finally to my family, especially my mother Elsa and grandparents Graciela and Roberto for supporting my academic pursuits, all this work is dedicated to all of you.

Glossary of Terms

AC: Awaji shima criteria
ALS: Amyotrophic lateral sclerosis
ALSFRS-R: Amyotrophic lateral sclerosis functional rating scale revised
BW: Bandwidth
CVD: cerebrovascular disease
DICOM: Digital Imaging and Communication in Medicine
FID: Free Induction decay
FLAIR: Fluid attenuated inversion recovery
GE: General Electric
GRE: Gradient Echo
HC: Healthy Controls
LMN: Lower motor neurons
LSQR: Sparse linear equation and least squares
MND: Motor Neuron Disease
MRI: Magnetic Resonance Imaging
PACS: Picture archiving and communication system
PLS: Primary lateral Sclerosis
PDF: Projection onto Dipole Fields
PMA: Progressive Muscular Atrophy
QSM: Quantitative Susceptibility Mapping
RF: Radio frequency
ROI: Region of interest
SE: Spin Echo
SHARP: Sophisticated Harmonic Artifact Reduction for Phase
SPGR: Spoiled gradient echo
SPSS: Statistical package for social science
STAR: Streaking artifact reduction
SWAN: Susceptibility Weighted Angiography

SWI: Susceptibility Weighted Imaging
SWIM: Susceptibility Weighted Imaging and Mapping
TE: Echo Time
TH: Slice thickness
TR: Repetition Time
UMN: Upper motor neurons

Contents

List of Figures

List of Tables

Chapter 1

Introduction

1.1 Motor Neuron Disease (MND)

Motor Neuron Disease (MND) is a rapidly progressive neurodegenerative disorder of the human motor system, it is defined as a neurological deterioration that increases over time [24]. This disorder is expressed in many forms, these are known as, progressive muscular atrophy (PMA), where motor neurons loss is restricted to only lower motor neurons (LMN)[25], Primary lateral Sclerosis (PLS), where motor neurons loss is instead, restricted to upper motor neurons (UMN) [25] and, Amyotrophic lateral sclerosis (ALS), which is the most common form and comprises both of PMA and PLS [25] disorders. Each form of MND was described independently, for example, ALS was originally described by Charcot in the 19th century [22]. PMA was described by François Aran in the middle of 19th century [27], and PLS was initially described by Wilhelm Heinrich Erb in 1875 [7]. Unfortunately this pathology has a median survival of three years and only 10 % of the patients survives over eight years [24]

1.1.1 MND in society

MND is a disease evenly distributed over the world [17], the mortality rate has ranged from 0.61/100.000 in Iceland to 2.4/100.000 in Sweden [10]. In the particular case of Italy, studies on different provinces have been conducted to understand the impact of the disease in the society.

One study in the province of Bologna, Italy, revealed that the mortality rate was 1.4/100.000 from 1986 to 1988 [10]. Other study in the province of Turin, Italy, for MND was found an annual incidence rate of 0.69 cases per 100.000 people and a prevalence of 2.62/100.000 from 1971 to 1980 [17]. In both studies, the results were standardized on the Italian population.

1.1.2 MND pathophysiology

The pathogenesis of a disease is the mechanism that causes the malfunctional state. In ALS, one of the main mechanisms operating in the pathogenesis is the iron overload, that leads to a metal-mediated oxidative stress, which causes cell damage [20] [28]. This overload means that the iron concentration is higher than the physiological quantity that can be stored and transported in the brain [28].

1.2 Clinical diagnosis

The diagnosis of MND is a long process and there is no single definitive test [24], this process involves careful clinical and neurological examination [24] during a long period of time to confirm the progress of the disease. *El Escorial* diagnostic criteria, which according to both peripheral and central neuron damage, defines four levels of diagnosis certainty [25]. According to the El escorial Criteria [2], the diagnosis of ALS requires the presence of:

- Evidence of LMN degeneration, by clinical, electrophysiological or neuropathologic examination.
- Evidence of UMN degeneration by clinical examination.
- Progressive propagation of symptoms or sings, to other regions of the body.

Together with the absence of:

- Electrophysiological or pathological evidence of other disease processes.
- Neuroimaging evidence of other disease processes.

However, El Escorial criteria has been updated with the pass of the years [25], this with the aim of increase the sensitivity of the method. For example, in 2008 a new diagnostic criteria $Awaji - shima\ criteria$ (AC) was published, where changes were made to the *El Escorial criteria* [12], the result was an increase in Electromyography sensitivity of AC.

On the other hand, a method to assess the severity of MND, is the Amyotrophic lateral sclerosis functional rating scale revised (ALSFRS-R) test, is a distributed score for the functional status of ALS patients, based on 12 items, each of them has a score from 0 to 4 [14], the final result is a number between 0 (maximum disability) and 48 (normal) points.

Magnetic resonance imaging (MRI) is routinely performed during the evaluation of patients to discard other possible diagnosis. In some clinical sequences (T_2-weighted and fluid attenuated inversion recovery (FLAIR)) signal alterations are observed in the motor regions of brain. Main alterations comprise hyperintense signals in the white matter and hypointense signals in the grey matter [15].

1.3 MRI Technique

1.3.1 MRI physics

Magnetic resonance imaging is one of the most known imaging techniques around the world. MRI relies on the property of nuclear spin, defined as the intrinsic *angular momentum* $\boldsymbol{L}$ of electrons, protons and neutrons [11], for MRI particularly in protons. Its necessary to remember that a moving charge is understood as a current, also that an electric current generates a magnetic field [6], measured in Tesla units. Therefore, protons have their own magnetic field, also called *magnetic moment* $\boldsymbol{\mu}$ [6]. The relation between these two quantities is given by *Gyromagnetic ratio* [11] and expressed in equation 1.1.

$$\mu = \gamma L \tag{1.1}$$

Without the presence of an external magnetic field, the protons are randomly orientated [6]. But in the moment that these are affected with an external magnetic field $\vec{\boldsymbol{B}}_{\mathbf{o}}$, the protons tend to orientate parallel

or anti-parallel to it [6] [3]. As the lowest energy state is parallel state, always parallel aligned protons are slightly more than antiparallel[6] to $\vec{\boldsymbol{B}}_{\mathbf{o}}$.

The overall result of a $\vec{\boldsymbol{B}}_{\mathbf{o}}$ applied on a group of protons, is a particular movement named *precession* [6] [3], this movement of the proton magnetic moment vector μ has an angular frequency described in equation 1.2.

$$\omega_0 = \gamma B_0 \tag{1.2}$$

The equation 1.2 is the Larmor equation [3], it relates the gyromagnetic ratio with the applied magnetic field, giving as a result the Larmor frequency $\boldsymbol{\omega}_{\mathbf{o}}$. All these protons precessing parallel (or antiparallel) to $\boldsymbol{B}_{\mathbf{o}}$ start to cancell out each other, only those extra protons that are parallel cause the magnetization effect seen macroscopically in the z-axis, along $\vec{\boldsymbol{B}}_{\mathbf{o}}$ [6]. This is called longitudinal magnetization $\boldsymbol{M}_{\boldsymbol{z}}$ with a value $\boldsymbol{M}_{\mathbf{o}}$ [6]. As the magnetization direction is the same of $\vec{\boldsymbol{B}}_{\mathbf{o}}$ no measurement can be performed [6] [3].

1.3.2 Radio frequency pulses

With the aim of measuring a signal, it is required to disturb the alignment of the protons with respect to $\vec{\boldsymbol{B}}_{\mathbf{o}}$ in a particular way. This is done with perpendicular Radio frequency (RF) pulses that have a magnitude $\boldsymbol{B}_{\mathbf{1}}$ [3] and the same frequency of precessional movement of the group of protons [6]. These pulses cause a gain in energy of the protons and in addition, generate a movement in phase of the protons (same direction at the same time) [6]. The interaction of the magnetization vector and the RF pulse applied is given by the equation 1.3, known as Bloch equation[3].

$$\frac{d\vec{M}}{dt} = \gamma \vec{M} \times \vec{B}_1 \tag{1.3}$$

The change in the orientation defines an angle, known as flip angle [3] and is described by equation 1.4.

$$\theta = \gamma B_1 \tau \tag{1.4}$$

If $\theta = 90°$ is called 90° Pulse. The term τ represents the duration of the RF pulse [3]. The result of these pulses are two effects [6], one is the reduction of the longitudinal magnetization, $\vec{M}_z$, because when protons

are excited with th RF pulse, there is a gain of energy, therefore, leave the parallel orientation to $\vec{\boldsymbol{B}}_{\mathbf{o}}$ going to an anti-parallel orientation, thus, the number of parallel and anti-parallel protons tends to be the same, causing the cancellation of their effect [6]. The second effect is that, these pulses, make the protons to move in phase, generating a new magnetization, called transverse magnetization $\vec{M}_{xy}$ [6] [3]

1.3.3 MRI measurements

Just when the RF pulse stops, the protons start to return to a lower energy state and to loss phase between them [6]. These processes are known as relaxation. These are defined in two ways, when the transverse magnetization is disappearing and when the longitudinal magnetization is returning to its original value. Both are processes that occur simultaneously and independently [6].

- **Spin-lattice interaction**: process related to the longitudinal magnetization [6][3], in this process the group of protons return to the original energy state at different times, the rate of change of M_z is proportional to the difference $M_0 - M_z$ [3], so plotting over time the value of longitudinal magnetization, it seen an exponential curve with a time constant **T1**, which describes how fast is this relaxation process [6]. Therefore, there is a restoration of the longitudinal magnetization [21]. The cause of this process is the exchange of energy between protons to return to their lower energy state [6]. As each tissue has different T_1 times, this property is used to differentiate them [6].

- **Spin-Spin interaction**: process related to the transverse magnetization, it describes the process where the protons stop being in phase in the x-y plane [6]. The transverse magnetization decreases in an exponential way and the time constant **T2** describes how fast reaches the 37% of its initial value [6]. This loss of phase is due to variations in the local precessional frequencies [3]. Is worth to say that for human tissues T_2 values are always smaller or equal than T_1 [6], also that T_2 time constant is significantly shorter in solid materials than in liquids.[3]

- **Spin-Spin interaction and field inhomogeneities** : Performing the T_2 measurements was observed that there is another source

of dephasing, the external field $\vec{\boldsymbol{B}}_{\mathbf{o}}$ inhomogeneities [3], the result of this effect is a shorter relaxation time, $T_2{*} < T_2$. This time constant takes into account the two causes of transverse magnetization decrease.

$$\frac{1}{T_2}* = \frac{1}{T_2} + \frac{1}{T_2}' \tag{1.5}$$

In equation 1.5, T_2 is the time constant saw above and the term T_2' represents the inhomogeneities of the external field, it is machine and sample dependent, but more important, it is recoverable [3], therefore, the dephase given from the inhomogeneities can be retrieved. This time constant is related to the estimation of iron concentration on the brain, and is presented in further sections.

The simplest MRI experiment consists in the measurement of a signal from a sample that has just received a RF pulse [3], this signal has its maximum just after the RF pulse ends, then rapidly decays and has an oscillation frequency $\boldsymbol{\omega}_{\mathbf{o}}$, this signal is called *Free Induction decay* (FID)[6]. Actually the $T_2{*}$ term mentioned above is the measure that determines the rate of decay in FID [6].

1.3.4 MR imaging methods

So far, the analysis is related only in time variation of signals. However, as MR is an image technique, it is required to measure how these signals change in space. As the same nuclei precess at different frequencies, according to the changes in the magnetic field in space, the local spatial distribution can be determined using the frequency information of the MR signal [3], This is done using a well-defined spatial variation [3] on the homogeneous field $\vec{\boldsymbol{B}}_{\mathbf{o}}$. This spatial variation is achieved providing three independent magnetic field gradients, named, *Slice Selection Gradient*, *Phase Encoding Gradient* and *Frequency Encoding Gradient* [6]. The key fact is that the measured signal, affected by a linear gradient, is the Fourier transform of the spin density along the axis of the gradient [3], therefore, to generate an image, two gradients are used, then, the measurements are stored, and finally, transformed to image space using inverse Fourier transform [3]. The spatial frequency space is also known as $k - space$ [6].

- **Phase encoding gradient**: named as Gp, consists in the use of

a gradient magnetic field that makes that some protons precess faster than other ones, depending on its position inside the gradient field. When the gradient is turned off, all the protons precess at the same frequency, but not in phase, which allows to differentiate the protons by its location. [6]. The spatial frequency related to the y-direction is given by equation 1.6

$$k_y = \gamma G_y \tau_y \tag{1.6}$$

- **Frequency encoding gradient**: named as Gf, is perpendicular to Gp gradient field, causing that the protons precess in a different frequency according to its position [6], the measurement of the MR signal is done during the time this gradient is on. The spatial frequency related to the x-direction is given by equation 1.7

$$k_x = \gamma G_x t' \tag{1.7}$$

Using these two gradients is possible to fill the $k - space$, using a RF pulse and a combination of gradients in k_x and k_y directions. There are several methods of filling the $k - space$, one of these, as is seen in figure 1.1, consist in the use of the gradients to sample all the values along a given slice of the sample. Initially is switched on the Gf, gradient in x direction, at the same time that the measurements are done. After a sample time T_S, is turned off and the phase encoding gradient is turned on, to move in vertical direction, then is turned off and again, is used Gf, but with negative polarity, to measure the following row. These steps are followed until the $k - space$ is filled [3].

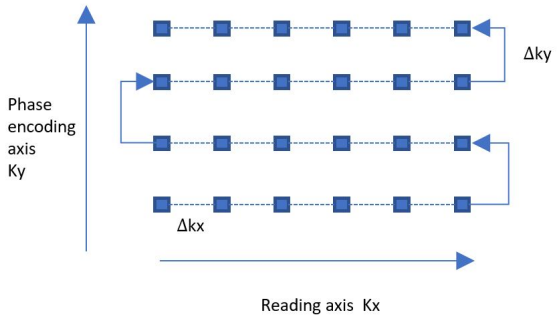

Figure 1.1: Encoding sequence example

- **Slice Selection** As the MRI is a technique that works on volumes, is necessary to generate images for different parts of the sample, each part is called slice. To measure these slices, is implemented a Slice selection gradient, which consists in the generation of a magnetic field along a chosen axis [6], let us call it slice axis. This axis is perpendicular to the plane of the desired slice, therefore, the result is a linear varying magnetic field along the slice axis [3]. The equation 1.8 expresses the change of the frequency along the slice axis, in this case z-axis,

$$f(z) = \gamma B_0 + \gamma G_z z \tag{1.8}$$

  Where γB_0 is the Larmor frequency at $z = 0$ [3]. Equation 1.8 represents the different Larmor frequencies that protons inside this field experiment. As the RF pulse does not have a unique frequency (band-limited), it excites just a slice with a certain thickness [6]. The bandwidth BW of the RF pulse is related to the slice thickness $TH = \Delta z$, with the equation 1.9

$$BW = \gamma G_z TH \tag{1.9}$$

1.3.5 MRI sequences

Mainly there are two image techniques that allow to measure MR images,

- **Spin-Echo (SE)**: It is an image technique based on the application of two different RF pulses. It has two main parameters *Echo Time* (TE), which is the time between the excitation pulse and the signal peak, and *Repetition Time* (TR), which is the time between two 90° excitatory pulses [6]. This sequence is divided in three steps, first is applied a 90° pulse, which creates a transverse magnetization M_{xy} and null longitudinal magnetization M_z at $t = 0$ [6]. After the RF pulse the different protons start to dephase, following 1.10

$$\phi(\vec{r}, t) = -\gamma \Delta B(\vec{r}) t \quad for \quad 0 < t < \tau \tag{1.10}$$

  The second step is at time $t = \frac{TE}{2}$, where a RF pulse of 180° is applied, so now, the phase in equation 1.10 changes its sign.

Therefore, the new phase is given by 1.11

$$\phi(\vec{r}, \tau^+) = \gamma \Delta B(\vec{r})\tau \tag{1.11}$$

In the third step, the spins keep losing phase coherence according to equation 1.10, as the rate in which the spins accumulate phase has not changed, is possible to compute the value of the phase after the 180° pulse [3].

$$\phi(\vec{r}, t) = -\gamma \Delta B(\vec{r})(t - 2\tau) \quad for \quad t > \tau \tag{1.12}$$

Where in equation 1.12 $2\tau \equiv TE$, therefore, for $t = TE$ the phase,is zero, $\phi = 0$. This null phase is known as realignment or also, as spin-echo [3], here M_{xy} has a maximum value.

- **Gradient Echo (GRE)**: It is an imaging sequence where only using a RF pulse and a magnetic gradient, is achieved a spin realignment. After the RF pulse excites the sample, a negative spatial gradient is applied, $G_z = -G$ for $G > 0$ [3], during a time interval (t_1,t_2). This phase shift process given by a gradient is given in equation 1.13

$$\phi_G(z, t) = -\gamma z \int_0^t G(t')dt' \tag{1.13}$$

According to equation 1.13 the phase in this interval is $\phi_G = +\gamma G_z(t_2 - t_1)$ [3]. Then, for the time interval (t_3,t_4) is applied a positive gradient. Therefore, having a phase

$$\phi_G = +\gamma G_z(t_2 - t_1) - \gamma G_z(t - t_3) \; for \; t_3 < t < t_4. \tag{1.14}$$

It is clear in 1.14 that there is a time t, when the phase returns to zero, this is at $t = t_3 + t_2 - t_1 \equiv TE$ [3], therefore at $t = TE$ occurs a realignment, known as Gradient Echo [3]. The GRE sequences usually are shorter than the SE[6].

1.3.6 MRI and magnetic susceptibility

The magnetic susceptibility is a property of the matter that can be measured with MRI images and it is related to metal concentrations. This property is represented with χ. In uniform materials, the magnetization vector $\vec{M}$ is proportional to magnetic field $\vec{H}$ [3], recall that

$\vec{B} = \mu\vec{H}$, where μ is the permeability, in other words, it describes how the material becomes magnetized [6], as described in equation 1.15.

$$\vec{M} = \chi\vec{H} \tag{1.15}$$

The susceptibility can be positive ($\chi > 0$) called paramagnetic, negative ($\chi < 0$) called diamagnetic, or ($\chi = 0$) for non magnetic materials [3]. The major part of the biological tissues cause weak diamagnetism, on the other hand, minerals like iron, cobalt or nickel show high values of susceptibility [6].

The most common imagine technique, to visualize susceptibility effects, is the spoiled gradient echo **SPGR** [18], whose magnitude images reflect the exponential T_2* decay and the phase images show the local frequency offset [18]. As was mentioned in subsection 1.3.3, the time constant T2* depends on T_2 and T_2', this last term has a relation with susceptibility [21], this contrast is seen because the refocusing only affects the T_2 term. Instead the T_2' effects remain affecting the signal and contrast [21].

Nowadays, magnetic susceptibility is commonly used in clinical practice by means of a technique called Susceptibility Weighted Imaging (SWI) which mainly relies on susceptibility differences to enhance contrast [18]. This technique combines the T_2*-weighted magnitude with a filtered phase image acquired with the gradient echo sequence [18]. The purpose for which this technique was implemented is the visualization of visualization of small vessels [18], furthermore, SWI proved to be sensitive to accumulations of molecules containing minerals, like copper or iron [18]. The SWI is retrieved by the multiplication of GRE magnitude and phase, nevertheless, the phase has to be unwrapped and filtered [18]. The result is an image with enhanced contrast between adjacent tissues with different values of magnetic susceptibility, useful to visualize blood vessels, calcifications and iron accumulation.

1.4 Quantitative Susceptibility Mapping (QSM)

As mentioned in subsection 1.3.6, the aim of using MR images is to measure or estimate iron concentration within a tissue. Unfortunately SPGR requires more steps to produce a quantitative measurement, this

is addressed with a processing technique called Quantitative Susceptibility Mapping (QSM) [18]. It is a noninvasive imaging technique to measure the spatial distribution of susceptibility using GREs images [5].

This processing method relies on phase images, so it has to be mentioned that there are several phase sources like iron, calcium, lipid and myelin content [8], but also, the phase changes depending on geometry and orientation [8] of the analyzed volume, with respect to $\vec{B_0}$. The goal of the technique is to only take into account source information of phase, thus, obtaining a source image [8]. The QSM is becoming a quantitative approach to characterize magnetic properties of brain tissues [5].

1.4.1 Mathematics

Assume the susceptibility induced magnetization χ as a magnetic dipole [5], therefore, the known field perturbation $\Delta B_z(\vec{r})$ is given by the convolution, in the image space, of the susceptibility distribution and the magnetic dipole kernel [5].

$\Delta B_z(\vec{r})$ is the variation of the field in the z-component, which is related to the magnetization source $M_z(\vec{r})$ [8] [9].

$$\Delta B_z(\vec{r}) = \frac{\mu_0}{4\pi} \int_{V'} d^3r' \left\{ \frac{3M_z(\vec{r'})(z-z')^2}{\left|\vec{r}-\vec{r'}\right|^5} - \frac{M_z(\vec{r'})}{\left|\vec{r}-\vec{r'}\right|^3} \right\} \tag{1.16}$$

Equation 1.16 is written as a convolution of the magnetization source $M_z(\vec{r'})$ with the point-dipole response $G(\vec{r})$ [8].

$$\Delta B_z(\vec{r}) = \mu_0 M_z(\vec{r}) * G(\vec{r}) \tag{1.17}$$

Where in equation 1.17 $G(\vec{r})$ is the spatial unit dipole [8] [9] which is defined in equation 1.18:

$$G(\vec{r}) = \frac{1}{4\pi} \frac{3\cos^2\theta - 1}{r^3} \tag{1.18}$$

The angle θ is measured between $\vec{r}$ and $\vec{z}$. The Fourier transform of the dipole Kernel in equation 1.18, is given by equation 1.19 [8]:

$$G(\vec{k}) = \begin{cases} \frac{1}{3} - \frac{k_z^2}{k^2}, & for \quad k \neq 0 \\ 0, & for \quad k = 0 \end{cases} \tag{1.19}$$

The dipole kernel is reported in figure 1.2

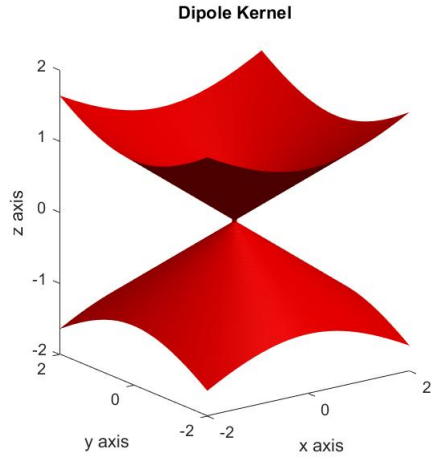

Figure 1.2: Plot of the Dipole kernel, implementing equation 1.19 on Matlab

Recall that if $\chi \ll 1$, $\mu_0 M_z(\vec{r}) \approx B_0\, \chi(\vec{r})$. Finally using the convolution theorem, $\Delta B_z(\vec{r})$ can be found as [5]

$$\Delta B_z(\vec{k}) = B_0 \left(\chi(\vec{k}) \cdot G(\vec{k})\right) \tag{1.20}$$

Where $\chi(\vec{k})$ is the Fourier transform of $\chi(\vec{r})$. This last term represents the susceptibility source distribution. After this mathematical review, is worth to mention that the goal of QSM is to find this susceptibility distribution, by solving the equation 1.20 as an inverse problem, where ΔB_z, B_0 and the dipole kernel $G(\vec{k})$ are known. The aim is to provide a pixel by pixel estimate of the susceptibility distribution, nevertheless, this is an ill-posed problem due to the zero values of the dipole kernel in $k - space$, thus inverse kernel is undefined at the canonical surfaces [5]. There are several algorithms proposed to solve this issue.

1.4.2 Artifacts

An artifact is defined as a spurious feature in a given image, occurs due to an imperfect data collection process or errors in data processing where approximations are made [3]. Two main artifacts are reviewed here

1. **Streaking artifacts**: Recall the dipole kernel in Fourier space 1.19, when is inverted (G^{-1}), to solve equation 1.20, it gives an ill-posed problem due to the null values of G along the magic angles [8]. The regions of ill-posed k-space are represented in the following image

Figure 1.3: Ill-posed regions of k-space, retrieved from [30]

   These artifacts may cause blurring of the edges and can be misinterpreted with anatomical tissues [8]. In the following image is seen an streaking artifact

   In the following subsections are reviewed some algorithms that reduce these artifacts.

2. **Blooming artifacts** Lets imagine a vessel orthogonal to the main field, assume inside the vein a phase of $-\pi/2$, in the edge a phase of $3\pi/2$. Because of the partial volume effects, the phases inside and outside the vessel are integrated across the voxel, leading to an increased T_2^* measurement. This causes in the images that smaller vessels seem to be thicker in the magnitude image, in the phase the given value is false [8].

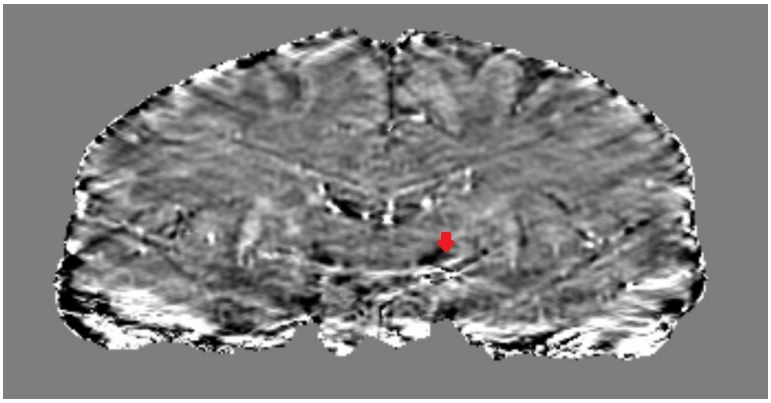

Figure 1.4: Streaking artifacts in QSM image from our database (coronal view)

1.4.3 QSM Main steps

The QSM computation is performed in several steps in order to deal the issues of an ill- posed problem:

1. **Phase Reconstruction**: In an MRI sequence that relies on phase images, a proper phase reconstruction is required. This implies to take into account the different sensitivities from the coils, chemical shift and phase induced by flowing spins [8]. Usually areused different channels to measure the phase, therefore, the different sensitivities from each channel have to be taken into account. Not taking into account these parameters may lead to incorrect data acquisition and thus, artifacts [9]. Mainly there are four types of multi-channel phase data combination algorithms [8].

    1.1. High-pass filtering method: To each image coming from each channel a high-pass filter applied, then the images are combined. Although the use of High-pass filter in the images is a robust and fast method, it has a drawback, and is the cancellation of the low frequency content in large structures [8].

    1.2. Phase difference method: To the phase images from each channel, a cancellation of the coil-sensitivity phase is performed. Then, these images are combined [8]. This method has the benefit that is done without doing phase unwrapping, but the drawback is a loss of signal to noise ratio (SNR) in

the combined phase images [8].

1.3. Global phase offset correction: a global constant phase offset is determined from each channel, using one channel as reference [8], then from each channel is removed this offset. Finally, the images are combined. Its seen that this method offers images with no cusp artifacts [8].

1.4. Coil-sensitivity correction: The coil-sensitivity induced phase is calculated for each channel, using phase from various echoes, and finally, removed from each channel before the combination. The drawback of this method is that requires the unwrapping of the phase from each channel at each echo, which is time-consuming [8].

2. **Phase unwrapping**: The recovered phase image may have wraps, so the aim of this step is to remove these wraps and recover the true phase. Nevertheless, this is another ill-posed problem because there are many true phase values that may lead to a wrapped value [23]. There are different approaches to solve this problem,

   2.1. Spatial unwrapping methods: these methods rely in the fact that phase has smooth changes between adjacent voxels, unless a wrap has occurred [23]. These can be divided into:

      2.1.1. Path-following methods: the assumption is, if there is a change greater of π in the phase of two adjacent voxels, a wrap has occurred. If there are no errors, this method is capable the exact value of the phase [23].

      2.1.2. Laplacian phase unwrapping: it has the goal to identify the unwrapped phase values, whose local derivatives are highly similar to the derivatives of the wrapped phase [23], therefore, this method is capable of removing the discontinuities. Nevertheless, it changes the phase values in a slow spatially way [23].

   2.2. Temporal unwrapping methods: uses the information available in several acquisitions, between echoes, to remove wraps that are time dependent [23]. It has the advantage that it is unaffected by the complexity of the wrapped image, but a

drawback, is that it is easily affected from noise compared to spatial methods [23].

To select the correct phase unwrapping algorithm is necessary to take into account that there is a trade-off between robustness and time-efficiency [8].

3. **Brain mask**: The idea is to use the magnitude image of the GRE sequence, with the objective of defining the volume of interest [8] (e.g. Cerebrum). A mask is used to do not take into account noisy regions with unreliable phase [8] that might generate artifacts in the computed susceptibility. The result is a binary image, where 1 values represent regions of interest and 0 values the unreliable regions.

4. **Removing background fields**: the phase in the image domain for a GRE sequence with a TE is given by equation 1.21 [8]

$$\phi(\vec{r}) = \phi_0(\vec{r}) + \gamma \Delta B_z(\vec{r}) TE \tag{1.21}$$

In equation 1.21 the term $\Delta B_z(\vec{r})$ represents the field variation and is expressed as the sum of the background field $\Delta B_b(\vec{r})$ and the local field $B_l(\vec{r})$ [8]:

$$\Delta B_z(\vec{r}) = \Delta B_l(\vec{r}) + \Delta B_b(\vec{r}) \tag{1.22}$$

In equation 1.22 the Background field ΔB_b is induced by the global geometry, interfaces and field inhomogeneities. In the other hand, the local field is generated by the susceptibility distribution. There are several algorithms to remove this background field

4.1. High-pass filtering method: this method consists in the application of a small 2D high-pass filter over the volume of interest. Then, a 1D high-pass filter in the missing dimension is applied, forming an effective 3D high-pass filter. Larger sized filter are avoided because it may affect $\Delta B_l(\vec{r})$, especially in large structures [8]

4.2. Geometry dependent artifact correction: in this algorithm the geometry of the air-tissue interfaces is retrieved from the magnitude image. Then, the background induced field from

these interfaces is estimated using the fast forward calculation of equation 1.23 [8].

$$\Delta B_{sinus}(\vec{r}) = B_0 FT \left\{ \sum \left[\chi_i(\vec{r}) \cdot g_i(\vec{r}) \right] \right\} \cdot G(\vec{k}) \tag{1.23}$$

Where $g_i(\vec{r})$ represents the geometry of the i^{th} sinus, with a constant susceptibility χ_i, $G(\vec{k})$ is the dipole equation in Fourier domain used in equation 1.19 and "$\cdot$" represents the point-wise multiplication [8]. This method has good performance depending on how good are extracted the geometries [8].

4.3. Dipole fitting, or better known as Projection onto Dipole Fields (PDF), it is a method where the background field inside a region of interest (ROI) is imposed using the dipoles outside the ROI [8] using the equation 1.24.

$$\Delta\chi_b(\vec{r}) = argmin_{\Delta\chi_b(\vec{r})} \left\| W \left[(\vec{r}) - B_0 \Delta\chi_b(\vec{r}) * G(\vec{r}) \right] \right\|_2^2 \tag{1.24}$$

Where $\Delta\chi_b(\vec{r})$ is the distribution of susceptibility of the point-dipole sources outside the brain, $\Delta B(\vec{r})$ is the measured field inside the brain, and finally, W is a weighting function derived from the magnitude images [8].

4.4. Sophisticated Harmonic Artifact Reduction for Phase (SHARP): Recall that the computation of $\chi(\vec{r})$ depends on the extraction of $\Delta B_l(\vec{r})$ from 1.22, also recalling $\Delta B_b(\vec{r})$ is generated by sources outside the volume of interest, therefore, it satisfies the Laplace's equation 1.25 throughout the volume [9].

$$\nabla^2 B_{ext} = 0 \tag{1.25}$$

On the other hand, as the contributions of $\Delta B_l(\vec{r})$ are inside the volume of interest, it can be found by solving the equation 1.26

$$\nabla^2 \Delta B_z(\vec{r}) = \nabla^2 B_l(\vec{r}) \tag{1.26}$$

Thus, is required to solve equation 1.26 for B_{int}, this is achieved using the equation 1.27 [9].

$$B_l = (\sigma - \rho) *^{-1} \Delta B \tag{1.27}$$

In equation 1.27 σ is the unit impulse at the center of the radial function, ρ is a non-negative, radially symmetric, normalized function [9].

5. **Solving the ill-posed inverse problem**: The susceptibility map is obtained by inverting equation 1.20. An approximation of $\widehat{G}^{-1}(\vec{k})$ with defined values is required [8], this process is called regularization. Usually this approximation implies a trade-off between the level of streaking artifacts and the underestimation of the susceptibility values [8]. In the next subsection are explained some of the more used algorithms which solve this ill-posed inverse problem.

1.4.4 Robust QSM tools

Nowadays algorithms are developed in software toolboxes whose inputs are the magnitude and phase images and the brain mask. Three main algorithms are reviewed:

- **SWIM**: Susceptibility Weighted Imaging and Mapping is an iterative sequence of steps in which at the ith step, the actual susceptibility map and the geometry of the veins is used to update the the k-space. Particulary the cone singularities are updated [8] to reduce artifacts. In a more detailed explanation this algorithm is described in seven steps [26]:

    1. The first step consists in the estimation of an initial susceptibility map $\chi_{i=0}(r)$, using a regularized form of the dipole kernel given in equation 1.19, therefore, values for indeterminate points in the kernel are defined [26].

    2. The geometry of the regions of interest is retrieved by multiplying $\chi_{i=0}(r)$ with a binary mask, where only the vessels are set to one, and other values, to zero. This is done knowing that usually the streaking artifacts are found outside the vessels [26]. The output is named $\chi_{vm,i}(r)$.

    3. The Fourier transform of $\chi_{vm,i}(r)$ is computed, giving $\chi_{vm,i}(k)$ [26].

    4. $\chi_{vm,i}(k)$ is multiplied by a binary mask that contains only unity values in the directions where $G(k)^{-1}$ is ill-conditioned, therefore, the result is the extraction of the information contained in $\chi_{vm,i}(k)$ but only in these directions. This output is called $\chi_{vm,cone,i}(k)$ [26].

5. Now the Fourier transform of $\chi_i(r)$ (i.e. $\chi_i(k)$) is summed with $\chi_{vm,cone,i}(k)$, therefore, part of $\chi_i(k)$ has been replaced. The new image is named $\chi_{merged,i}(k)$ [26].

6. The inverse Fourier transform for $\chi_{merged,i}(k)$ is computed. It gives an improved susceptibility map $\chi_{i+1}(r)$ [26]

7. The susceptibility map used in step one is replaced with the one obtained in step 6.

The vessels mask used in step 2, is generated using a threshold method, this is, all the voxels, in the used image in step 1 $\chi_{i=0}(r)$, with a susceptibility value higher than a value, are set to one and the others, to zero [26].

- **ILSQR**: in few words, it is a method that uses a sparse linear equation and least squares (LSQR) algorithm, to obtain an initial estimate of susceptibility. It also uses a fast QSM method to stimate susceptibility boundaries. The innovative step is the interative process to compute the streaking artifacts from ill-conditioned k-space regions [29]. Finally, the computed streaking artifacts are subtracted from the original image [30].

  1. Initial estimate of susceptibility, the LSQR method solves the equation 1.28 [30].

  $$G \cdot FT(W_1\psi) = GFT\left[W_I \cdot FT^{-1}\left\{G \cdot FT(\chi_{LSQR})\right\}\right] \quad (1.28)$$

  Where the term W_1 is a weighting function to reduce artifacts due to inaccurate phase unwrapping [30] and G is the Fourier transform (FT) of the dipole, used in 1.19. The output of this step is named χ_{LSQR}, from this image, in the final step, are subtracted the artifacts.

  2. Next, the binary mask for $k - space$ is computed, where the ill-conditioned regions have unity value and the other regions have zero value. It is named M_{IC} [30].

  3. To estimate the susceptibility boundaries, first, the susceptibility contrast is computed, these boundaries are used in the next step to compute the weighting masks W_{Gi}. In [30] this method is called fast QSM method. The first step is to estimate a susceptibility contrast based on the sign of G and

the normalized phase [30] following equation 1.29.

$$\chi_{F1}(k) = sign(G) \cdot FT(\psi) \tag{1.29}$$

From this rough estimation a discontinuity at $G = 0$ is obtained. To correct this discontinuity, the discontinuous data in k-space is averaged along the surface, then this k-space data is transformed into an image using the inverse Fourier transform (FT^{-1}). This step is reported in the equation 1.30 [30].

$$\chi_{F2} = FT^{-1}\left\{\chi_{F1}(k) \cdot W_{FS} + F\left[\chi_{F1}(k)\right] \cdot (1 - W_{FS})\right\} \tag{1.30}$$

The term F, represents the average operation applied to remove the discontinuity. In the other hand, W_{FS} is an empirically function found that has the objective of limiting the averaging over the ill-conditioned regions [30]. To define W_{FS}, is necessary to determine first, the constant term in equation 1.31.

$$W_0 = \frac{|G|^{0.001} - a}{b - a} \tag{1.31}$$

Where a is the first percentile value of $|G|^{0.001}$ and b, the 30th [30], then, the function W_{FS} is defined according to the conditions [30] in equation 1.32:

$$\begin{cases} W_{FS} = 0, & W_0 < 0 \\ W_{FS} = W_0, & 0 < W_0 < 1 \\ W_{FS} = 1, & 1 < W_0 \end{cases} \tag{1.32}$$

The result of equation 1.30 still has streaking artifacts in the regions outside the brain that can be removed by multiplying with a mask. This masked image is transformed into Fourier space, with the aim of spreading the masking effects into different frequency components [30], also a second averaging of the k-space is applied. Finally the image is transformed back to image space and multiplied again with the mask. This is seen in equation 1.33.

$$X_{F3} = FT^{-1}\left\{FT\left(M \cdot \chi_{F2}\right) \cdot W_{FS} + F\left[FT\left(M \cdot \chi_{F2}\right)\right](1 - W_{FS})\right\} \cdot M \tag{1.33}$$

Where M represents the binary image for the tissue of interest.

The output image named χ_{FS} is obtained from equation 1.34

$$\chi_{FS} = a \cdot \chi_{F3} + b \tag{1.34}$$

Where the values of a and b are the used above.

4. From the image χ_{FS} are computed the weighting functions $W_{\nabla i}$ following equation 1.35 [30].

$$\begin{cases} W_{\nabla i} = 1, \quad \nabla_i(\chi_{FS}) < \nabla_{i,min} \\ W_{\nabla i} = \frac{|\nabla_{i,max} - \nabla_i(\chi_{FS})|}{|\nabla_{i,max} - \nabla_{i,min}|}, \nabla_{i,min} < \nabla_i(\chi_{FS}) < \nabla_{i,max} \\ W_{\nabla i} = 0, \quad \nabla_{i,max} < \nabla_i(\chi_{FS})) \end{cases} \tag{1.35}$$

Then, it is possible to find the susceptibility artifacts (SA) by solving the equation 1.36.

$$min_{\chi_{SA}(k)} \sum_i \left\| W_{\nabla i} \cdot \nabla_i \left\{ \chi_0 - FT^{-1} \left[\chi_{SA}(k) \cdot M_{IC} \right] \right\} \right\|_2 \tag{1.36}$$

Equation 1.36. leads to the generation of the image with the susceptibility artifacts named χ_{SA}. Where χ_0 is an initial susceptibility estimated from 1.29. i represent the axes x, y and z, ∇_i are gradient operators, $G_{i,max}$ and $G_{i,min}$ are the thresholds for gradient weight calculation.

5. Subtraction of streaking artifacts.

$$\chi_{iLSQR} = \chi_{LSQR} - FT^{-1} \left[\chi_{SA}(k) \cdot M_{IC} \right] \tag{1.37}$$

- **Streaking artifact reduction (STAR)** QSM-STAR algorithm reduces streaking artifacts using a two level regularization method, reconstructing large and small susceptibility values. It is worth to say that the process is all automatic. First the algorithm computes the susceptibility from isolated strong sources [29]. The field of these sources is estimated with the forward equation, and then, subtracted from the total phase [29]. The result of the subtraction is used to find the susceptibility from the weaker sources. The result is superimposed onto the strong susceptibility obtained before, improving the QSM quality [29].

The normalized phase $\psi = \phi/\gamma\mu_0 H_0 TE$ with ϕ as the phase measured at a given TE, has a relationship with the magnetic susceptibility following equation 1.38

$$\psi = FT^{-1}\left\{G \cdot FT(\chi)\right\} \tag{1.38}$$

G is the Fourier transform of the magnetic dipole kernel, but in equation 1.39 is defined as the discrete version [29].

$$G = FT\left\{\frac{\Delta r_x \cdot \Delta r_y \cdot \Delta r_z\left[3 \cdot (\hat{H} \cdot r)^2 - (r_x^2 + r_y^2 + r_z^2)\right]}{4\pi(r_x^2 + r_y^2 + r_z^2)^{\frac{5}{2}}}\right\} \tag{1.39}$$

In equation 1.39, r represents the position vector, r_i the spatial coordinates and Δr_i, represent the size of the voxel, $\hat{H}$ is the used magnetic field vector [29].

The goal of STAR-QSM, is to solve the equation 1.40

$$\chi = min\left\{\left\|FT^{-1}(G\ dotFT(\chi)) - \psi\right\|_2 + \lambda\left\|W \cdot \nabla \cdot \chi\right\|_1\right\} \tag{1.40}$$

The L1 norm, in 1.41, calculates the overall variation of the weighted gradient. The term λ is a regularization parameter that its value depends on the spatial smoothness and consistency of the data [29]. This norm is given by equation 1.41.

$$\left\|W \cdot \nabla \cdot \chi\right\|_1 = \sqrt{(W_{\nabla x} \cdot \nabla_x \cdot \chi)^2 + (W_{\nabla y \cdot \chi} \cdot \nabla_y)^2 + (W_{\nabla z} \cdot \nabla_z \cdot \chi)^2} \tag{1.41}$$

This method is described in the following steps:

1. First, equation 1.40 is solved with a large value of λ, this leads to an estimation of only strong susceptibility sources.
2. Then, the dipole field corresponding to the strong susceptibility sources is determined by the forward equation 1.38
3. Next, the computed dipole field is subtracted from the total phase.
4. Now is possible to determine the susceptibility map from the residual phase that corresponds to weaker sources, using a smaller λ parameter
5. Finally, the susceptibility maps obtained in step one and step four are superimposed having as a result the final QSM image with large dynamic range.

Finally it is seen that all the algorithms reconstruct the susceptibility maps by different methods. The three algorithms have in common that these by different methods reconstruct the Fourier transform of the susceptibility map, to then retrieve the susceptibility map. Each algorithm consider different methods to overcome the undefined values of the dipole kernel. Particularly, QSM-STAR has a different approach in the reconstruction of susceptibility map. As suggested in [29], the STAR algorithm has a significantly better performance in reducing streaking artifacts, compared to ILSQR.

1.5 Quantitative Susceptibility Mapping in MND state of art

Two main studies served as guidelines to develop this work. *Ji Young Lee* studied the differences in motor cortex susceptibility between three groups of participants (Amyotrophic lateral sclerosis (ALS), cerebrovascular disease (CVD), and healthy controls), looking for significant differences among them [16]. This study found that the QSM is a potentially useful technique to be implemented as imaging biomarker for ALS, due to significantly high QSM values in the motor cortex, this aimed us in the develop of the project. Nevertheless, this study has the limitation that the regions of interest were drawn manually, thus time-consuming and operator dependent [16].

Also was found that M. Costagli developed a study looking for a correlation between QSM values with an Upper motor neuron impairment score, more exactly to demonstrate that signal variation in T_2^* images, of ALS patients, corresponds to an increase of iron concentration [19]. This study was relevant because of the established workflow, the QSM images were obtained using a Laplacian-based phase unwrapping and applying a SHARP background phase removal [19], finally, susceptibility χ was found using ILSQR method. Nevertheless, this study has the same problem that the ROIs were drawn manually. M. Costagli presented as a result, that QSM might prove useful in estimating iron concentration as a possible radiological sign of UMN burden in ALS patients [19].

1.6 Project Aim

Due to the high incidence and mortality of MND described in [17] and [10] and the sensibility of MRI to iron overload, we decided to implement a fully automatic pipeline able to quantify susceptibility in the motor cortex in three pathological groups, ALS, PLM and PMA, and one group of Healthy controls. Then, test for differences in susceptibility measurements among the groups and establish a relationship between susceptibility measurements and the clinical scores.

Chapter 2

Methods

2.1 Subject groups

The group of participants was comprised 51 *MND* and 25 *Healthy Controls* (HC). The MND group is subdivided into 36 *ALS patients*, 6 *PLS patients* and 9 *PMA patients*. The clinical diagnosis was performed by the Department of Neurology in the *Istituto Auxologico Italiano San Luca* hospital. Whole group age data are summarized in table 2.1.

Group	**Mean Age**	**Age Standard deviation**	**Age Range**	**Male**	**Female**
Healthy Subjects	57.92	7.78	44-73	9	17
MND	61.21	9.63	41-78	23	28
ALS	60.86	9.02	42-74	17	19
PMA	61.88	13.34	41-76	5	4
PLS	62.33	8.35	55-78	1	5

Table 2.1: Group anagraphic data

2.2 Image acquisition

Whole-brain images were acquired in a 3T General Electric (GE) SIGNA scanner. T1-weighted images had the following parameters: Repetition time=8.7ms, Echo time=3.2ms, Pixel spacing=0.5mm, Slice thick-

ness=1mm, spacing between slices=1mm, flip angle=12°, Rows=512, Columns=512. Susceptibility Weighted Angiography (SWAN), providing phase and magnitude images, had the following parameters: Repetition time=39ms, 7 equally spaced echoes centered at 24ms, Pixel spacing=0.468mm, Slice thickness=1.4mm, spacing between slices=0.7mm, flip angle=20°, Rows=512, Columns=512. By default phase images were high-pass filtered by the machine for clinical purposes. These images were assessed by a radiologist and a resident of radiology from the neuroradiology Deparment of *Ospedale Policlinico di Milano*.

2.3 Image processing Pipeline

In figure 2.1 is showed the implemented fully-automatic Pipeline described in this thesis work, each step is described in the following sections.

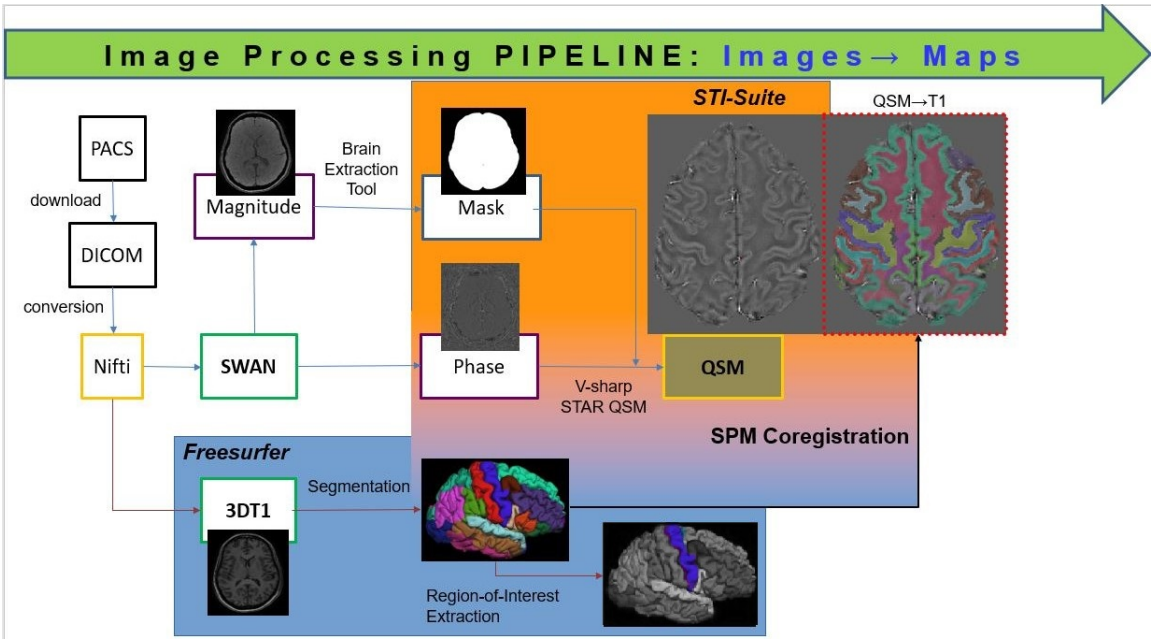

Figure 2.1: Fully automatic pipeline

2.3.1 Preprocessing

T1 Sagittal image and Axial SPGR image in magnitude and phase were used in the image process pipeline. Initially, images stored in Digital Imaging and Communication in Medicine (DICOM) [13] format were retrieved from the Picture Archiving and Communication System *PACS* of the hospital. PACS is a technology tool which provides communication and storage of images, from different users. This allows easy exchange of medical images between different machines. Then, images were converted into NifTI format, using "dcm2nii" functions in MATLAB (R). This step was needed to decrease image size and to allow reading from processing tools. The images that were required are shown in figure 2.2.

The brain masks were obtained using "FSL" software, as recommended in [30] and [9].

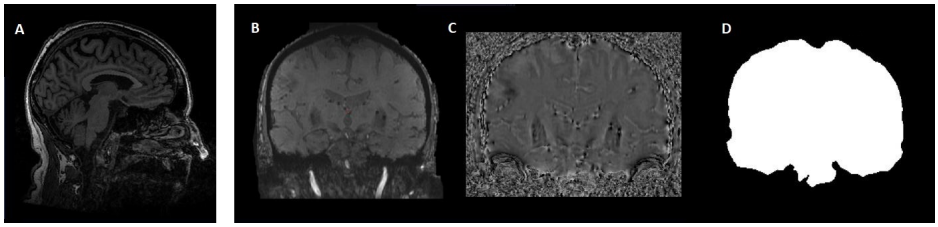

Figure 2.2: (A) Sag T1 image and ax (B) Magnitude (C) Phase (D) and Mask images

2.3.2 QSM test and reconstruction

The main three tools described in subsection **1.4.4** where applied to the data with the aim of choosing the one with better performance. The optimal parameters needed in each software were defined in collaboration with the relative developing group (i.e. Wayne State University for SMART tool and University of California Berkeley for STI Suite tool). An illustrative quantitative susceptibility map is shown in figure 2.3, while the different outputs of the described algorithms are presented in the results section.

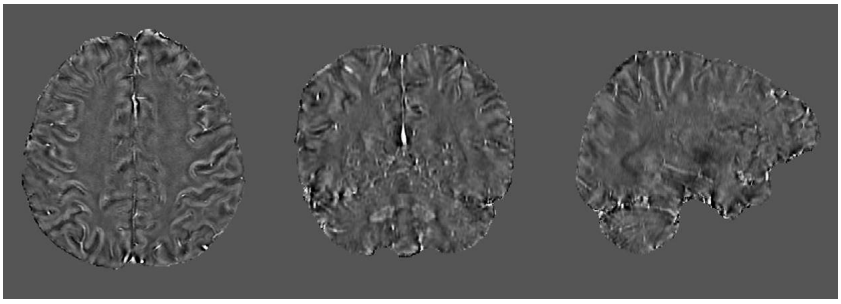

Figure 2.3: QSM image

2.3.3 Segmentation and volumetric information

The anatomical T1 images were segmented using FreeSurfer automatic segmentation. This is a robust process, where the different brain structures were accurately identified. This software requires as input the anatomical image and gives as output a labeled brain image, where a number is assigned for each brain structure in each hemisphere. An example of labeled brain is reported in figure 2.4.

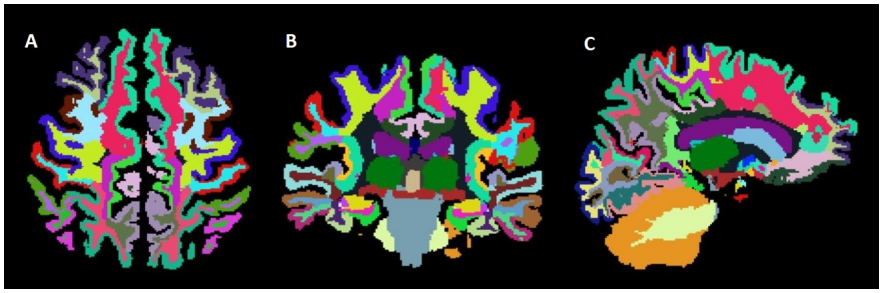

Figure 2.4: Labeled Brain

FreeSurfer also allows to perform different geometric measurements in the different segmented structures, so the cortical thickness and the area of the cortical structures were measured as an additional step. The mean thickness and area in left and right hemispheres were used to calculate the mean thickness in both hemispheres using formula 2.1.

$$\overline{Thickness}_{both} = \frac{Thickness_{left} * Area_{left} + Thickness_{right} * Area_{right}}{Area_{left} + Area_{right}} \tag{2.1}$$

2.3.4 Coregistration

Small movements may occur between the acquisition of the anatomical T1 images and the magnitude/phase images. Thus, a coregistrarion was required, specially because the regions of interest are very small (i.e. 2-4mm of width). The Matlab Toolbox SPM12 provides the algorithms to perform this task and overcome the small mismatch between images. SPM allows to choose a *reference* image, a *source* image, which is the one that is fitted into the *reference* image and *other* images, which are images that are fitted as the *source* image.
The anatomical T1 image was chosen as *reference* image, the magnitude image was chosen as *source* image and finally, the QSM image was chosen as *other* image. As QSM and magnitude are in the same space, all changes done in magnitude were applied also to the QSM map. Finally, the output was a QSM map that matched spatially with the anatomical image T1, which also implied that matches with the labeled brain image. The resulting registered QSM image with labeled brain is reported in figure 2.5.

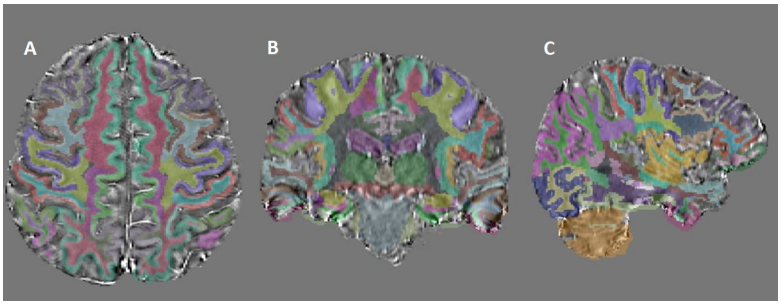

Figure 2.5: Labeled QSM Brain

2.3.5 ROI extraction

Motor cortex comprises the brain areas involved in the process of voluntary motion. It is distributed over a large region located in the precentral gyrus. Motor cortex is usually represented as is seen in figure 2.6, where each region represents a specific area of motor control.

In our labeled brain, motor cortex is subdivided in two regions (i.e. Precentral and Paracentral), as illustrated in figure 2.7 (A1 and A2).

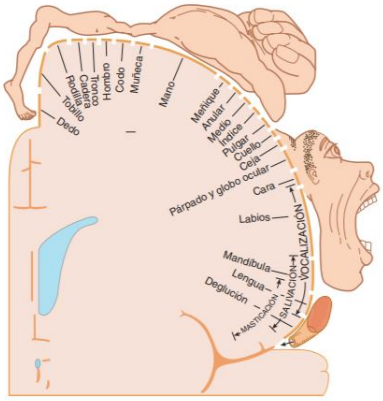

Figure 2.6: Cortical motor homunculus, image from [1]

After the regions of interest extraction, we decided to joint these sections, as figure 2.7 illustrates in (B1 and B2) and (C1 and C2). Finally in figure 2.7 (D1 and D2) an example of extracted ROIs from susceptibility map, is illustrated

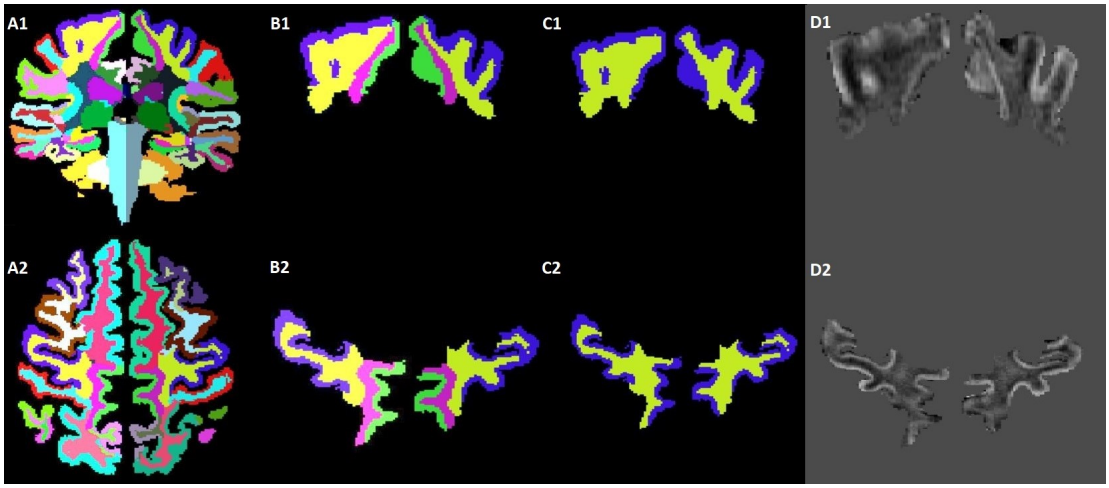

Figure 2.7: ROI extracted, (A) Segmented anatomical brain image (B) Extracted regions from anatomical image (C) Joint of both regions (D) Same regions in susceptibility map

2.3.6 Susceptibility and morphovolumetric metrics

The measurements performed in the region of interest were

- In the susceptibility map:
    1. Mean.
    2. Skewness.
- In the anatomical image:
    1. Thickness.
    2. Area.

2.4 Statistical tests

Statistical package for social science (SPSS) was used to analyze data as recommended in [16] and in [15]. Student t-test was used to compare age, cortical thickness, mean susceptibility values in cortex and in subcortical white matter, susceptibility skewness in cortex and subcortical white matter between MND and HC. ANOVA was performed to compare the above mentioned metrics among the clinical subgroups and HC. When ANOVA reached significance, post-hoc tests were performed. Then, Pearson correlation analyses between measured variables and age were performed in MND and HC separately. In MND, further Pearson correlation analyses were performed between the measured neuroimaging variables and disease duration and ALSFRS-R.

Chapter 3

Results

First, an illustrative quantitative susceptibility map of each algorithm is shown, then another illustrative example of the background field removal algorithm is shown. Next results of group age differences are reported and the results of statistical tests in Neuroimaging measurements are presented. Finally, results of correlation test between neuroimaging measurements an clinical results are reported.

3.1 Susceptibility Maps

The output image from each software is shown in the figure 3.1, for the same subject were applied the reviewed algorithms (SWIM, ILSQR and STAR)

3.2 Background field removal

The result of the use of a Background removal algorithm in susceptibility computation are presented in figure 4.2. This Background field removal was applied to images obtained with QSM STAR algorithm.

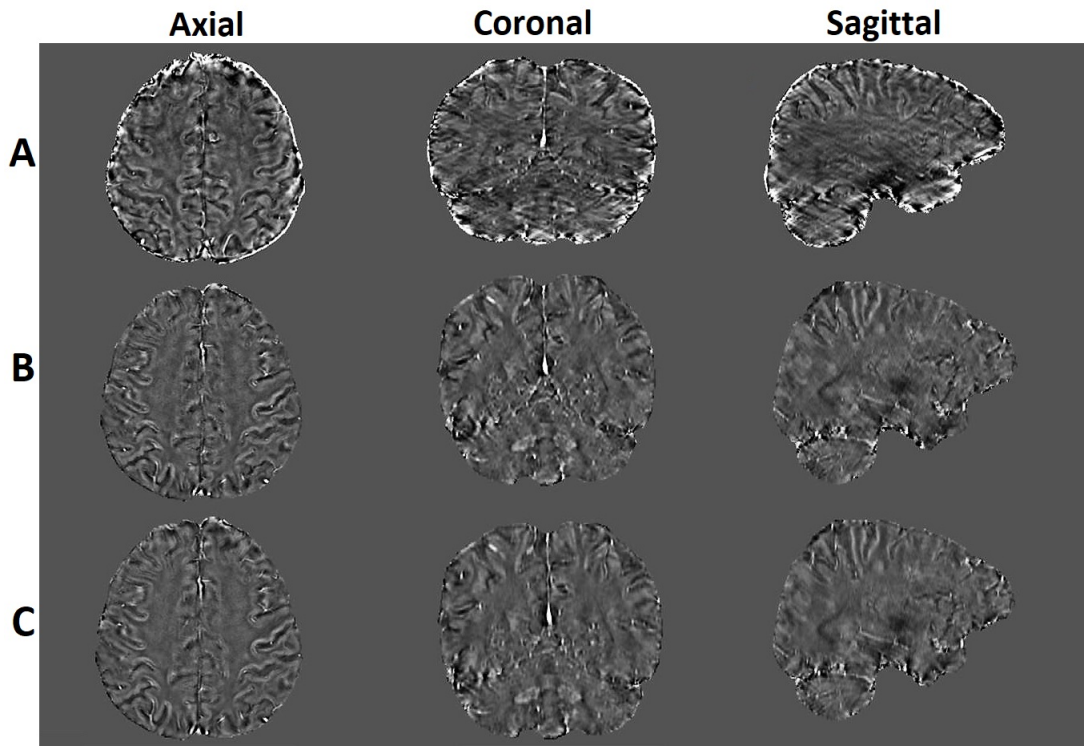

Figure 3.1: Susceptibility maps computed with (A) SMART SWIM (B) STIsuit ILSQR (C) STIsuit STAR

3.3 Age differences among groups

Age did not statistically differ between MND and HC ($p = 0.078$), among subclinical groups and between each subclinical group and HC ($Sig = 0.354$).

3.4 Neuroimaging measurements in MND

Mean thickness in MND was significantly lower than HC ($p = 0.0001$). ANOVA test revealed differences among subclinical groups and HC ($Sig = 0.001$) and Post-Hoc tests indicated differences between ALS and HC ($p = 0.001$) and between PLS and HC ($p = 0.0001$).

Mean susceptibility in cortical region was not statistically different between MND and HC ($p = 0.139$), and among subclinical groups and HC ($Sig = 0.088$).

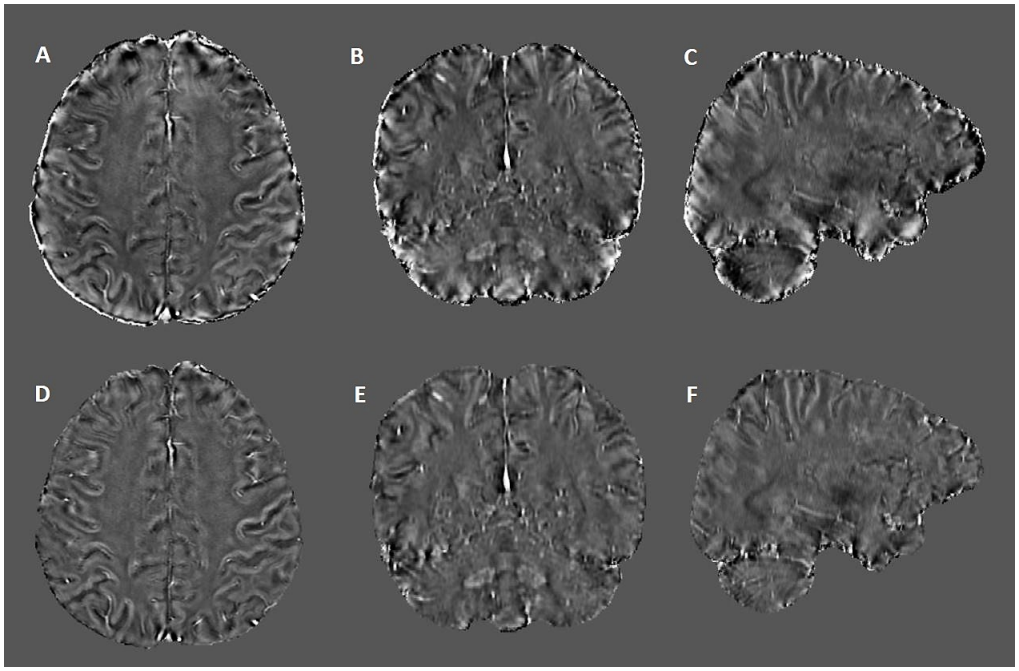

Figure 3.2: Susceptibility maps with and without Background removal

Mean susceptibility in subcortical white matter was significantly higher in MND compared to HC ($p = 0.005$). ANOVA test suggested a borderline significance comparing subclinical groups and HC ($Sig = 0.059$) and Post-Hoc tests gives $p = 0.052$ between ALS and HC, $p = 0.0079$ between PLS and HC and $p = 0.004$ between PMA and HC.

Skewness of the susceptibility distribution in cortical region was significantly higher in MND compared to HC ($p = 0.002$). ANOVA test revealed differences among subclinical groups and HC ($Sig = 0.0001$), and Post-Hoc tests indicated differences between ALS and HC ($p = 0.007$), ALS and PMA ($p = 0.014$), and PLS and HC ($p = 0.0001$).

Skewness of the susceptibility distribution in subcortical white matter was not statistically different between MND and HC ($p = 0.05$), and among subclinical groups and HC (0.416).

3.5 Neuroimaging measurements and clinical variables correlation

In HC, age showed a statistically significance correlation with mean susceptibility in cortical region ($Sig = 0,042$, $r = 0.35$), skewness in cortical region ($Sig = 0.17$, $r = 0.42$) and skewness in subcortical white matter ($Sig = 0.19$, $r = 0.42$). In HC, cortical thickness did not show any significant correlation with the measured variables.

In MND, age showed a statistically significant correlation with cortical thickness ($Sig < 0.000$, $r = -0.55$), mean susceptibility in cortical region ($Sig < 0,000$, $r = 0.49$), and skewness in subcortical white matter ($Sig = 0.011$, $r = 0.32$). In MND, cortical thickness showed a statistically significant correlation with mean susceptibility in subcortical white matter ($Sig = 0,000$, $r = -0.53$), skewness susceptibility in cortical region ($Sig < 0.000$,$r = -0.24$) and in skewness subcortical white matter ($Sig < 0,0002$, $r = -0.51$). In MND, disease duration showed a significant correlation with mean susceptibility in subcortical white matter ($Sig = 0.033$,$r = 0.26$). ALSFRS showed a statistically significant correlation with cortical thickness ($Sig = 0.007$, $r = 0.40$) and mean subcortical white matter ($Sig = 0.026$, $r = -0.42$).

Chapter 4

Discussion

MND is a group of progressive neurological disorders that destroy motor neurons, where different pathological phenotypes with different symptoms are included. Indeed, MND presents motor impairment in different body regions (i.e. upper limb and/or lower limb) mapped in the brain motor cortex. We were interested in studying the iron accumulation in the motor cortex and the anomalies in subcortical white matter adjacent to the motor cortex. For this purpose we used QSM, the tool able to quantify iron accumulation and changes in myelin, by measuring the local susceptibility.

Thus, we decided to implement a fully automatic method that could deal the different phenotypes uniformly. This method had to include the motor cortex in its mesial, dorsal and ventral regions, potentially affected by the pathology. This was according to the intensity variation in susceptibility sensitive MR images reported by physicians in these regions.

A visual comparison between the algorithms SWIM, ILSQR and STAR allows to see how different algorithms with the same inputs, generate different susceptibility maps. Clear differences arose between SWIM and both ILSQR/STAR algorithm. Instead, ILSQR and STAR images seemed to be quite similar. Therefore we decided to subtract both images, to reveal differences among them, this is reported in figure 4.1. The resulting images revealed the features present only ILSQR output map. A set of streaking artifacts that is seen in figure 4.1 confirms that STAR algorithm has a better performance than ILSQR algorithm.

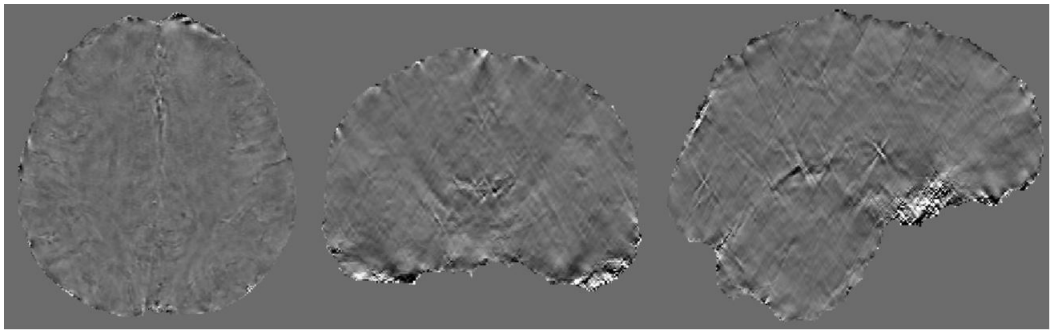

Figure 4.1: Susceptibility maps ILSQR and STAR subtraction

Furthermore we decided subtract the generated images from the same patient and from same algorithm, one of these with background removal (e.g. SHARP) algorithm and the other without it, this is reported in figure 4.2. This procedure revealed the impact of this algorithm, it clearly removed noise from borders.

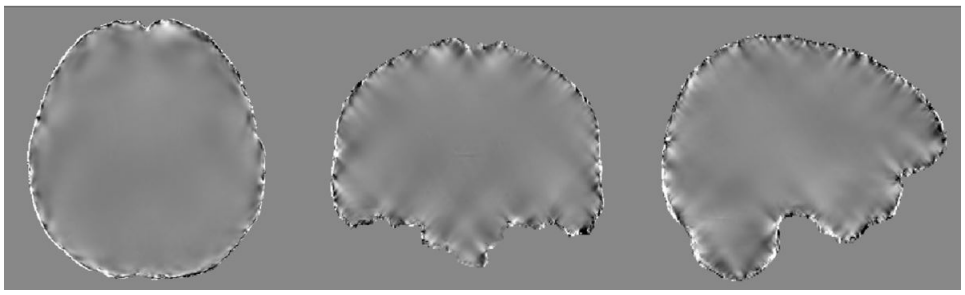

Figure 4.2: Background field removal on STAR susceptibility map

A statistical comparison between MND and HC revealed that cortical thickness, white matter susceptibility (mean and skewness) and cortical skewness susceptibility are significantly different. Cortical thickness analysis confirms the expected reduction in cortical thickness widely described in literature. The evidences of this thesis work confirm previous studies on the topic and provides a more detailed characterization.

Indeed, the susceptibility skewness seems to be much more sensible to cortical anomalies than mean susceptibility over the cortical region. We believe that correlation between age and mean susceptibility and the absence of correlation of age with the skewness could provide an explanation (i.e. Skewness does not depend on age). The skewness of the cortical susceptibility could be a more reliable measurement than

mean susceptibility in wide age range studies.

The results in the white matter assessment are interesting and less expected than the ones in gray matter. From a neuroradiologic point of view, physicians often observe hyperintensity in these cortical regions and less frequently in subcortical white matter. No previous quantitative studies analyzed subcortical white matter susceptibility adjacent to motor cortex. The subcortical white matter presents a significant difference between MND and HC, in both mean and skewness, suggesting that susceptibility variations in the white matter are also occurring.

The direction of the change is coherent with the expected changes. The increment of susceptibility in cortical regions could be related to the iron accumulation and the less negative susceptibility values in the subcortical white matter could be related to loss of myelin characterized by diamagnetic properties.

As described in literature, the more probable phenotype in MND is ALS [4]. We did confirmed the much higher percentage of ALS over PLS and PMA in our MND population.

As ALS and PLS refer in literature [24] to a deterioration of upper motor neurons, which dendrites lies in motor cortex, we expected that there should have been significant differences between ALS patients and HC as well as between PLS and HC. Instead, between ALS and PLS we did not expect any significant difference as both pathologies present upper motor neuron impairment. These hypotheses were confirmed as both ALS and PLS present significant differences with HC in cortical susceptibility skewness and cortical thickness. Instead, among ALS and PLS there is no statistical difference.

Instead, PMA vs HC revealed an interesting and unexpected result, the mean white matter in subcortical region reveals a relevant difference between these groups, this results suggested that the use of white matter to differentiate these groups could be more meaningful.About correlation in HC, cortical thickness did not correlate with cortical susceptibility (mean and skewness) and subcortical white matter susceptibility (mean and skewness). This might suggest that in normal conditions these two variables are not dependent.

In the other hand, interesting correlations between the cortical thickness and cortical susceptibility skewness, and with subcortical white

matter susceptibility mean and skewness were observed in MND.

For the clinical correlations in the MND group, the functional score ALSFRS-R has an interesting correlation with cortical thickness and with mean subcortical white matter susceptibility. This suggests that both cortical thickness and mean subcortical white matter may reflect the functional conditions in MND patients.

Disease duration revealed an unexpected but interesting result, a correlation with mean susceptibility in subcortical white matter. This reaffirmed our believes that measurements in subcortical white matter might be meaningful in MND studies.

About the age there are two important facts that have to be highlighted. First, for the consistency of the study was important to have a set of participants such that the age of each group should not show any significance difference, with the aim to discard that age is a variable affecting our measurements. This was reached taking into account either the whole MND group and the single clinical subgroup compared to HC.

On the other hand, in the HC group, the fact that there is a correlation between age and mean cortical susceptibility is relevant, because it confirms studies where an increase of susceptibility with the pass of the years independently to any pathology was shown. In addition, our study suggests that the cortical and subcortical susceptibility skewness correlates with age in the healthy control group.

The automatic pipeline allows to quantify magnetic susceptibility in all the cortical regions defined in the Desikan-Killiany Atlas and the other subcortical regions of Freesurfer. Thus, a whole-brain study could be easily performed as extension of this thesis. Therefore, this pipeline could be applied to several neurodegenerative disorders, where iron accumulation is expected and a quantification is desired.

Our pipeline was applied on a clinical dataset which included a whole-brain scan with a standard resolution in the z-axis (T_1 $1mm$ and $SPGR$ $1.4mm$ with a spacing between slices of $0.7mm$). This resolution is still very low when working on cortical regions which have a width between $2mm$ and $4mm$. Thus, our pipeline had to deal with partial volume effects, which might alter the measurement of susceptibility within a voxel. A specific acquisition protocol focused on the cortex

could provide additional evidences. As a susceptibility quantification has been achieved, it would be interesting to build a "supermetric" equation based on age, cortical thickness and susceptibility skewness variables that according to its result, might suggest the presence of anomalies.

On the other hand, in order to have more meaningful results is required to enlarge the study, including pathological control group, to determine the specificity of the evidences.

A relevant part of this work is that, the regions of interest were defined automatically, overcoming the dependence of the selected region to ability of the operator and achieving a property of reproducibility not available in handmade regions of interest. The fact of being fully automatic leads to a property of reproducibility that has not been seen in other quantitative susceptibility studies in MNDs.

It is worth to mention that MND diagnostic procedures requires an MRI scan to exclude other pathologies. Thus, the implemented pipeline might not require any additional exam. Furthermore, QSM only requires a multiecho gradient-echo sequence, commonly included in clinical protocols.

Chapter 5

Conclusions

For the first time, a fully automatic neuroimaging pipeline has been developed and applied to study the susceptibility properties of the motor cortex and relative subcortical white matter in MND. Skewness of susceptibility distribution in the motor cortex could be a more sensitive measurements than the mean value to assess iron overload in MND. Furthermore, our study suggest that the assessment of subcortical white matter susceptibility might enrich the characterization of the pathologic tissue in MND. And its role in defining an MRI biomarker for MND should be further investigated

The here presented pipeline might be easily adapted to automatically quantify susceptibility in every brain region, in MND or any other neurodegenerative disease.

Chapter 6

Appendix

Age distribution		
Comparison	**P value**	**Anova**
MND vs HC	0.078	
ANOVA		0.354

Table 6.1: Summary results of age distribution

Cortical susceptibility mean		
Comparison	**P value**	**Anova**
MND vs HC	0.139	
ANOVA		0.088

Table 6.2: Summary results cortical susceptibility mean

Cortical susceptibility skewness			
Comparison	**P value**	**Anova**	**Post-Hoc**
MND vs HC	0.002		
ANOVA		0.0001	
ALS vs HC			0.007
ALS vs PLS			0.014
ALS vs PMA			0.086
PLS vs PMA			0.001
PLS vs HC			0.0001
PMA vs HC			0.768

Table 6.3: Summary results cortical susceptibility skewness

White matter susceptibility mean			
Comparison	**P value**	**Anova**	**Post-Hoc**
MND vs HC	0.005		
ANOVA		0.059	
ALS vs HC			0.052
ALS vs PLS			0.755
ALS vs PMA			0.271
PLS vs PMA			0.590
PLS vs HC			0.079
PMA vs HC			0.004

Table 6.4: Summary results White matter susceptibility mean

White matter susceptiblity skewness		
Comparison	**P value**	**Anova**
MND vs HC	0.04	
ANOVA		0.416

Table 6.5: Summary results White matter susceptibility skewness

Mean Thickness of precentral and paracentral regions			
Comparison	**P value**	**Anova**	**Post-Hoc**
MND vs HC	0.0001		
ANOVA		0.001	
ALS vs HC			0.001
ALS vs PLS			0.145
ALS vs PMA			0.504
PLS vs PMA			0.068
PLS vs HC			0.0001
PMA vs HC			0.120

Table 6.6: Summary results Precentral and Paracentral regions thickness mean

ALSFRS-R Correlations					
Comparison	**Cortical Thickness**	**Mean cortical susceptibility**	**Mean subcortical susceptibility**	**Skewness cortical susceptibility**	**Skewness subcortical susceptibility**
ALSRS-R	0.4	0.14	-0.31	-0,14	-0.09
Sig	0.007	0.21	0.031	0.199	0.294

Table 6.7: Results of ALSFRS-R correlations

Disease duration Correlations					
Comparison	**Cortical Thickness**	**Mean cortical susceptibility**	**Mean subcortical susceptibility**	**Skewness cortical susceptibility**	**Skewness subcortical susceptibility**
Disease Duration	-0.15	-0.17	0.26	-0,09	0.07
Sig	0.141	0.110	0.033	0.258	0.317

Table 6.8: Results of disease duration correlations

Age Correlations in MND group					
Comparison	**Cortical Thickness**	**Mean cortical susceptibility**	**Mean subcortical susceptibility**	**Skewness cortical susceptibility**	**Skewness subcortical susceptibility**
Age	-0.53	0.49	0.11	0.06	0.32
Sig	>0.000	>0.000	0.215	0.339	0.011

Table 6.9: Results of age correlations in MND group

Age Correlations in HC group					
Comparison	**Cortical Thickness**	**Mean cortical susceptibility**	**Mean subcortical susceptibility**	**Skewness cortical susceptibility**	**Skewness subcortical susceptibility**
Age	-0.22	0.35	0.12	0.42	0.42
Sig	0.149	0.042	0.276	0.017	0.019

Table 6.10: Results of age correlations in HC group

Cortical thickness correlations MND group				
Comparison	**Mean cortical susceptibility**	**Mean subcortical susceptibility**	**Skewness cortical susceptibility**	**Skewness subcortical susceptibility**
Cortical Thickness	-0.22	-0.53	-0.24	-0.51
Sig	0.064	>0.000	0.043	>0.000

Table 6.11: Results of cortical thickness correlations MND group

Cortical thickness correlations in HC group				
Comparison	**Mean cortical susceptibility**	**Mean subcortical susceptibility**	**Skewness cortical susceptibility**	**Skewness subcortical susceptibility**
Cortical Thickness	-0.08	-0.15	0.01	-0.11
Sig	0.352	0.237	0.478	0.305

Table 6.12: Results of cortical thickness correlations in HC group

References

[1] Kim E. Barrett, Susan M. Barman, Scott Boitano, Heddwen L. Brooks, and Michael Weitz. Ganong's review of medical physiology. New York : McGraw Hill Education, [2016] ©2016, 2016.

[2] Brooks, Benjamin Rix and Miller, Robert G. and Swash, Michael and Munsat, Theodore L. El Escorial revisited: Revised criteria for the diagnosis of amyotrophic lateral sclerosis. Amyotrophic Lateral Sclerosis and Other Motor Neuron Disorders, 2000.

[3] Brown, Robert W. and Cheng, Yu Chung N. and Haacke, E. Mark and Thompson, Michael R. and Venkatesan, Ramesh. Magnetic Resonance Imaging: Physical Principles and Sequence Design. Wiley Blackwell, 2014.

[4] National Clinical Guideline Centre. Motor Neurone Disease: Assessment and Management. National Clinical Guideline Centre (UK), 2016.

[5] Chunlei Liu and Hongjiang Wei and Nan-Jie Gong and Matthew John Cronin and Russel Dibb and Kyle Decker. Quantitative Susceptibility Mapping: Contrast Mechanisms and Clinical Applications. In Tomography, 2015.

[6] Currie, Stuart and Hoggard, Nigel and Craven, Ian J. and Hadjivassiliou, Marios and Wilkinson, Iain D. Understanding MRI: basic MR physics for physicians. Postgraduate Medical Journal, 2013.

[7] Doctor Frans Brugman and Professor John Wokke. Primary lateral sclerosis. Orphanet, 2002.

[8] E. Mark Haacke and Saifeng Liu and Sagar Buch and Weili Zheng

and Dongmei Wu and Yongquan Ye. Quantitative susceptibility mapping: current status and future directions. Magnetic Resonance Imaging, 2015.

[9] Ferdinand Schweser and Andreas Deistung and Berengar Wendel Lehr and Jurgen Rainer Reichenbach. Quantitative imaging of intrinsic magnetic tissue properties using MRI signal phase: An approach to in vivo brain iron metabolism? NeuroImage, 2011.

[10] Ferro, S. and Giovannini, A. and Fiorani, L. and Carmentano, P. and D Alessandro, R. Mortality from motor neuron disease in the province of bologna, italy, 1986 through 1988. Archives of Neurology, 1992.

[11] Freude, Dieter. Spectroscopy for Physicists (English version). Chapters 3 - 4.

[12] Jeffrey M. Statland and Richard J. Barohn and April L. McVey and Jonathan S. Katz and Mazen M. Dimachkie. Patterns of Weakness, Classification of Motor Neuron Disease, and Clinical Diagnosis of Sporadic Amyotrophic Lateral Sclerosis. Neurologic Clinics, 2015.

[13] Charles E. et al. Kahn. Dicom and radiology: Past, present, and future. Journal of the American College of Radiology, 2007.

[14] Kollewe, Katja et al. ALSFRS-R score and its ratio: A useful predictor for ALS-progression. Journal of the Neurological Sciences, 2008.

[15] Kwan, Justin Y. Iron Accumulation in Deep Cortical Layers Accounts for MRI Signal Abnormalities in ALS: Correlating 7 Tesla MRI and Pathology. plos one, 2012.

[16] Lee, J. Y. and Lee, Y. J. and Park, D. W. et al. Quantitative susceptibility mapping of the motor cortex: a comparison of susceptibility among patients with amyotrophic lateral sclerosis, cerebrovascular disease, and healthy controls. Neuroradiology, 2017.

[17] Leone, M. and Chio, A. and Mortara, P. and Rosso, M. G. and Schiffer, D. Motor neuron disease in the Province of Turin, Italy, 1971-1980. Acta Neurologica Scandinavica, 1983.

[18] Liu, Chunlei and Li, Wei and Tong, Karen A. and Yeom, Kris-

ten W. and Kuzminski, Samuel. Susceptibility-weighted imaging and quantitative susceptibility mapping in the brain. Journal of Magnetic Resonance Imaging, 2015.

[19] M. Costagli and G. Donatelli and L. Biagi and E. Caldarazzo Ienco and G. Siciliano and M. Tosetti and M. Cosottini. Magnetic susceptibility in the deep layers of the primary motor cortex in Amyotrophic Lateral Sclerosis. NeuroImage: Clinical, 2016.

[20] Maria Teresa Carri and Alberto Ferri and Mauro Cozzolino and Lilia Calabrese and Giuseppe Rotilio. Neurodegeneration in amyotrophic lateral sclerosis: the role of oxidative stress and altered homeostasis of metals. Brain Research Bulletin, 2003.

[21] Markl, Michael and Leupold, Jochen. Gradient echo imaging. Journal of Magnetic Resonance Imaging, 2012.

[22] Michael Strong and Jeffrey Rosenfeld. Amyotrophic lateral sclerosis: A review of current concepts. Amyotrophic Lateral Sclerosis and Other Motor Neuron Disorders, 2003.

[23] Robinson, Simon Daniel and Bredies, Kristian and Khabipova, Diana and Dymerska, Barbara and Marques, Jose P. and Schweser, Ferdinand. An illustrated comparison of processing methods for MR phase imaging and QSM: combining array coil signals and phase unwrapping. NMR in Biomedicine, 2016.

[24] Simon, N. G. and Huynh, W. and Vucic, S. and Talbot, K. and Kiernan, M. C. Motor neuron disease: current management and future prospects. Internal Medicine Journal, 2015.

[25] T. Lenglet and J.-P. Camdessanche. Amyotrophic lateral sclerosis or not: Keys for the diagnosis. Revue Neurologique, 2017.

[26] Tang, J. and Liu, S. and Neelavalli, J. and Cheng, Y. C. N. and Buch, S. and Haacke, E. M. Improving susceptibility mapping using a threshold-based K-space/image domain iterative reconstruction approach. Magnetic Resonance in Medicine, 2013.

[27] Visser, Jeldican and de Jong, J. M. B. Vianney and Visser, Marianne de. The history of progressive muscular atrophy. Neurology, 2008.

[28] Wang, Yi and Spincemaille. Clinical quantitative susceptibility

mapping (QSM): Biometal imaging and its emerging roles in patient care. Journal of Magnetic Resonance Imaging, 2017.

[29] Wei, Hongjiang and Dibb, Russell and Zhou, Yan and Sun, Yawen and Xu, Jianrong and Wang, Nian and Liu, Chunlei. Streaking artifact reduction for quantitative susceptibility mapping of sources with large dynamic range. NMR in Biomedicine, 2015.

[30] Wei Li and Nian Wang and Fang Yu and Hui Han and Wei Cao and Rebecca Romero and Bundhit Tantiwongkosi and Timothy Q. Duong and Chunlei Liu. A method for estimating and removing streaking artifacts in quantitative susceptibility mapping. NeuroImage, 2015.